ACADÉMIE
DES SCIENCES
INSTITUT DE FRANCE

Comptes Rendus
Mécanique

Benjamin Favier and Patrice Le Gal

Bénard–von Kármán–Taylor–Proudman phantom wakes

Volume 354 (2026), p. 783-800

Online since: 9 September 2026

https://doi.org/10.5802/crmeca.379

CENTRE MERSENNE
The Comptes Rendus. Mécanique *are a member of the Mersenne Center for open scientific publishing*
www.centre-mersenne.org — e-ISSN : 1873-7234

ACADÉMIE DES SCIENCES
INSTITUT DE FRANCE

Comptes Rendus. Mécanique
2026, Vol. 354, p. 783-800
https://doi.org/10.5802/crmeca.379

Research article

Bénard–von Kármán–Taylor–Proudman phantom wakes

Benjamin Favier [*, a] **and Patrice Le Gal** [a]

[a] Aix Marseille Univ., CNRS, Centrale Med, IRPHE, Marseille, France
E-mails: benjamin.favier@cnrs.fr, legal@irphe.univ-mrs.fr

Abstract. The Bénard–von Kármán wake is a canonical phenomenon in fluid mechanics, readily identified by its alternating vortex street forming behind a bluff body. Seemingly unrelated, rapidly rotating fluids give rise to elongated, quasi-two-dimensional structures known as Taylor columns. The Taylor–Proudman theorem indeed enforces an invariance of the flow along the rotation axis when inertial and viscous effects are small compared with Coriolis forces. Here, we combine these two seemingly distinct phenomena by studying the formation of what we call phantom wakes: a rotating fluid appears to flow around a non-existent solid obstacle, namely a Taylor column. We address the question of whether a Bénard–von Kármán-type wake can spontaneously emerge under such conditions. To do so, we perform direct numerical simulations of an imposed flow in a rotating channel containing a small cylindrical cavity on one wall, which generates a Taylor column. By systematically varying the Rossby and Reynolds numbers, we analyze the progressive emergence of a wake behind the column and its convergence toward the classical vortex street. As in the non-rotating case, vortex shedding occurs through a Hopf bifurcation, which we characterize for a fixed Rossby number. However, the transition threshold varies non-monotonically with rotation. For intermediate Rossby numbers, elliptical streamlines and a shorter recirculation region are observed, resulting in a critical Reynolds number exceeding the classical value of 47. These findings not only reveal unexpected wake dynamics, but also suggest a mechanism for Taylor column formation that depends sensitively on the cavity geometry.

Keywords. Rotating flows, Taylor column, wakes, stability, bifurcation.

Manuscript received 29 April 2026, revised 13 July 2026, accepted 14 July 2026, online since 9 September 2026.

Introduction

The interaction between a solid obstacle and a flowing fluid leads to some of the most studied and recognizable phenomena in fluid dynamics. In particular, it is common knowledge that a fluid flow past a circular cylinder becomes unstable beyond a critical Reynolds number, giving rise to the well-known Bénard–von Kármán vortex street, named after Henri Bénard [1,2] and Théodore von Kármán [3,4]. Since then, a large body of work has been devoted to this wake [5], including the description of its bifurcation characteristics [6,7], its spatial structure [8], and the prediction of vortex shedding frequency [9], to cite a few representative more recent works on the subject.

Some years after Bénard's seminal observations, and on a seemingly unrelated topic, Taylor [10] and Proudman [11] derived what is now known as the Taylor–Proudman theorem, which states that a slowly moving object in a rapidly rotating fluid must drag along the entire fluid column lying above and below it. This surprising result was actually derived earlier by Hough [12]

* Corresponding author

and observed even before by Kelvin in 1868 [13], finally leading to the famous experimental observations made by Taylor [14] himself of what are now called Taylor columns.

Combining these two milestones of fluid dynamics — the Bénard–von Kármán wake on the one hand and the Taylor–Proudman theorem on the other hand — leads to the field of rotating wakes. These wakes are of interest in some geophysical situations, such as large-scale wakes behind islands [15,16], and there is today a growing interest in the effect of topography on geophysical fluid dynamics [17].

A survey of the literature shows that several important distinctions must be made between different types of rotating wakes. A first distinction concerns the fluid domain. The present study deals with a bounded domain, in contrast to the numerous studies devoted to objects moving in unbounded rotating fluids [18–20]. A second distinction concerns the geometry of the obstacle. Some studies consider obstacles extending across the entire fluid channel, whereas others focus on finite-size obstacles. For full-span cylindrical obstacles, the wake dynamics also depend on the orientation of the cylinder axis relative to the rotation axis. When the two axes are perpendicular, the wake is dominated by inertial waves [21,22] (see also [23] for inclined cylinders in stratified fluids). When they are aligned, background rotation alters the vortex-shedding dynamics. This latter configuration has been extensively investigated, from the pioneering experiments of Boyer [24–27] to more recent studies on rotating shallow-water wakes [28] and elliptical instabilities [29,30]. In contrast, the present work considers the wake generated by a finite-size obstacle moving perpendicular to the rotation axis in a bounded fluid domain.

Starting from the early experiments of Taylor [14,31], many authors have explored the spontaneous emergence of a Taylor column around a finite-size object slowly moving across a bounded rotating fluid. We focus here on the case where the obstacle moves perpendicular to the rotation axis, and do not consider motion parallel to the axis [20,32–35]. Different flow regimes are observed depending on the relative importance of inertia, rotation, and viscous effects, usually quantified by the Rossby and Reynolds numbers. The geometric parameters of the object, such as its aspect ratio between horizontal and vertical sizes or the ratio between its height and the depth of the fluid domain, are also of importance. The experiments of Hide [36], later confirmed by Heikes and Maxworthy [37], showed that a Taylor column can emerge provided that the Rossby number is small compared to the ratio between the height of the obstacle and that of the fluid channel, which was later confirmed theoretically by Ingersoll [38] and Huppert [39], and numerically by Mason and Sykes [40]. In the slender-body limit, Stewartson and Cheng [41] theoretically showed that the response takes the form of a Taylor column provided that the Rossby number is sufficiently small compared to the ratio between the horizontal size of the obstacle and the depth of the fluid domain. In all cases, a fluid column with vanishing velocity in the rotating frame is attached to the moving obstacle providing that the Rossby number is small enough. What happens to the Taylor column once it has formed has also attracted the attention of experimental and numerical studies [42–44].

Other important complications can arise in confined rapidly rotating fluids when viscosity is taken into account. One such complication is the presence of Ekman boundary layers along the horizontal no-slip walls of the fluid channel [45]. These layers can significantly affect the development of the wake behind the obstacle, and may even completely suppress flow detachment behind the solid object when the Rossby number is much smaller than the square root of the Ekman number [24,46–48]. Even when detachment occurs and wake dynamics develops, Ekman friction on the bounding horizontal plates can strongly damp the vortex shedding behind the object [26,29], further complicating comparisons between rotating wakes and classical free two-dimensional wakes. Another complication is the topographic β effect induced by the non-uniform fluid depth characteristic of free-surface fluid experiments for instance. While relevant to atmospheric situations, the importance of this global topographic effect further complicates the analysis of the wake, which can then radiate Rossby waves [29,43,49].

In an attempt to simplify the problem as much as possible, we choose here to explore the wake behind a Taylor column free from viscous effects within the Ekman layers induced by the two horizontal plates confining the rotating fluid. Moreover, we will adopt the classical f-plane approximation with a constant fluid depth. Thus, we will consider the spontaneous formation of a Taylor column that appears above a circular cylindrical cavity, and more specifically in the subsequent instability of the wake behind this Taylor column, which may eventually lead to a Bénard–von Kármán-like vortex street (see Figure 1(a)). The closest study relevant to our particular case is that of Boyer et al. [43], who observed the destabilisation of the Taylor column behind a cylindrical depression. To better establish a link between the classical Bénard–von Kármán vortex street and the destabilisation of a Taylor column, we employ three-dimensional direct numerical simulations, which allow us to consider a stress-free rotating fluid channel, thus preventing the emergence of Ekman boundary layers for the reasons explained above. In this configuration, we anticipate a possible convergence between this three-dimensional problem and the classical two-dimensional Bénard–von Kármán wake problem as the Rossby number decreases. The numerical formulation is described in Section 1, while the main results are presented in Section 2. Finally, we conclude with a discussion in Section 3.

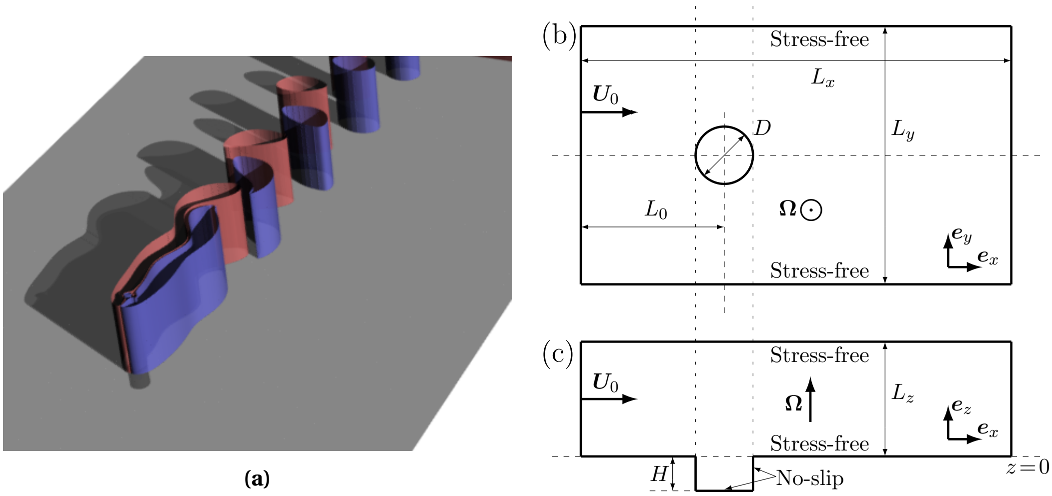

Figure 1. (a) Isocontours of the vertical vorticity for a phantom wake at Ro = 10^{-3} and Re = 70. The flow is shown in a top view, with the grey surface representing the bottom plate; the cylindrical cavity beneath is visible through transparency. Although no solid obstacle is present within the channel, the Taylor column originating from the cavity inhibits fluid entrainment by the mean flow, thereby producing a vortex street downstream of the phantom obstacle. Schematic of the configuration of interest viewed from the top (b) and the side (c).

1. Formulation and methods

1.1. *Mathematical formulation*

We solve the Navier–Stokes equations for an incompressible fluid in a rotating frame with constant rotation rate $\boldsymbol{\Omega} = \Omega \boldsymbol{e}_z$. The domain is a rectangular channel of width L_y and height L_z with stress-free side boundary conditions, preventing the development of Ekman and Stewartson boundary layers. In the streamwise direction, the channel has a length L_x and we impose a uniform velocity $U_0\boldsymbol{e}_x$ both at the inlet and at the outlet of the channel, thereby imposing a constant mass flux through the channel. Note that in this formulation, the Coriolis acceleration acting on the mean imposed flow is balanced by a transverse pressure gradient maintained by the impenetrable side boundaries of the channel. Without additional ingredients, this configuration leads to a stationary and uniform flow everywhere across the channel. A small cylindrical cavity, flush with the bottom boundary of the channel, of diameter D and height H, is placed at the bottom of the channel at distance L_0 from the entrance of the channel, with no-slip boundary conditions on its vertical and bottom boundaries. See Figure 1(b) for a global view of the configuration of interest.

Using D as a reference length scale and $1/\Omega$ as a reference time scale, the dimensionless Navier–Stokes equations in the rotating frame are

$$\frac{\partial \boldsymbol{u}}{\partial t} + \boldsymbol{u}\cdot\nabla\boldsymbol{u} + 2\boldsymbol{e}_z \times \boldsymbol{u} = -\nabla P + \mathrm{E}\nabla^2\boldsymbol{u}, \tag{1}$$

$$\nabla\cdot\boldsymbol{u} = 0. \tag{2}$$

The problem is principally controlled by the Ekman and Rossby numbers defined as

$$\mathrm{E} = \frac{\nu}{\Omega D^2} \quad \text{and} \quad \mathrm{Ro} = \frac{U_0}{\Omega D}, \tag{3}$$

where ν is the constant kinematic viscosity of the fluid. The Reynolds number based on the diameter of the cavity is simply

$$\mathrm{Re} = \frac{U_0 D}{\nu} = \frac{\mathrm{Ro}}{\mathrm{E}}. \tag{4}$$

In this paper, we will systematically vary both the Reynolds and the Rossby numbers in the range $\mathrm{Re} \in [40;300]$ and $\mathrm{Ro} \in [10^{-3};0.3]$. In addition to these two dimensionless parameters, the configuration depends on five geometrical dimensionless parameters:

$$\lambda_x = \frac{L_x}{D}, \quad \lambda_y = \frac{L_y}{D}, \quad \lambda_0 = \frac{L_0}{D}, \quad \lambda_z = \frac{L_z}{D} \quad \text{and} \quad h = \frac{H}{D}. \tag{5}$$

In order to avoid any confinement effects, the first three parameters need to be large enough to avoid significant effects from the inlet, outlet and side boundary conditions on the flow development around the cylinder. While true unconfined dynamics require excessively large domains [50,51], we take $\lambda_x = 50$, $\lambda_y = 30$ (streamwise and lateral extent of the channel in diameter units) and $\lambda_0 = 15$ (distance between the inflow boundary conditions and the cylinder in diameter units) which is a reasonable compromise between numerical costs and converging towards unconfined wake dynamics. In particular, the typical wake wavelength as measured by experiments [52] is around $\lambda/D \approx 6$, significantly smaller than both λ_0 and λ_x. The two important remaining geometrical parameters that we consider here are the height of the channel along the rotation axis λ_z and the depth h of the cylindrical cavity below the main channel. λ_z is a known important parameter when it comes to the transition to quasi two-dimensional dynamics in rapidly-rotating flows and the formation of Taylor columns [36]. In this paper, we will take $\lambda = 4$ but systematically vary the Rossby number to trigger the transition between a regime dominated by inertial waves and that dominated by a Taylor column. Note that we measure the height h with respect to the channel bottom located at $z = 0$ so that a flush depression corresponds to $h < 0$ and an obstacle protruding inside the channel corresponds to $h > 0$. While most of our simulations will use $h = -1$, so that the height of the cylindrical depression is equal to its diameter, we will nevertheless vary this parameter in Section 2.6 below (and compare the case of a depression with that of an obstacle $h > 0$, as in [43]).

The boundary conditions on the channel side boundary are all stress-free:

$$\frac{\partial u_x}{\partial z}=\frac{\partial u_y}{\partial z}=u_z=0 \quad \text{for } z=0,\lambda_z, \tag{6}$$

$$\frac{\partial u_x}{\partial y}=\frac{\partial u_z}{\partial y}=u_y=0 \quad \text{for } y=-\lambda_y/2,\lambda_y/2, \tag{7}$$

thus preventing the formation of Ekman (resp. Stewartson) boundary layers on the horizontal (resp. vertical) plates bounding the channel. In addition, no Ekman pumping will alter the vortex sheet which will eventually develop behind the depression. As previously stipulated, we impose no-slip boundary conditions on both the flat bottom boundary and the vertical side boundary of the cylindrical depression:

$$\boldsymbol{u}=\boldsymbol{0} \qquad \text{for } z=h \text{ and } \sqrt{x^2+y^2}\le 1, \tag{8}$$

$$\boldsymbol{u}=\boldsymbol{0} \qquad \text{for } h\le z\le 0 \text{ and } \sqrt{x^2+y^2}=1. \tag{9}$$

At the entrance and at the exit of the channel, a uniform velocity is imposed, ensuring a constant mass flux through it:

$$\boldsymbol{u}=\mathrm{Ro}\,\boldsymbol{e}_x \quad \text{for } x=-\lambda_0 \text{ and } x=\lambda_x-\lambda_0. \tag{10}$$

In order to smoothly transition from the flow behind the cylinder to the uniform outflow boundary condition, we use a thin sponge layer in which a relaxation term gradually damps fluctuations about the imposed uniform base flow. This sponge layer is only acting at a distance of one diameter from the outlet which we recall is located at 35 diameters from the cylindrical cavity. We have found no effect of this sponge layer on the wake dynamics, and it prevents spurious flows near the fixed velocity exit of the channel. Finally, it is important to note that the transition between the stress-free channel and the no-slip cylindrical obstacle is rather singular. The fluid can freely slip along the bottom horizontal wall until it reaches the cylindrical cavity where a no-slip boundary condition is imposed. We have ensured that our global solution does not depend on the specifics of the numerical discretisation around this transition. We have in particular use significantly enhanced local resolution around the cylindrical cavity (see Section 1.2 below). We used different initial conditions, from flow at rest with a gradual increase of the imposed flow speed to restart from statistically-stationary simulations at different control parameters, and we did not observe any dependence on the initial conditions.

1.2. *Numerical methods*

We use the open-source spectral element code Nek5000 [53–55] which has already been extensively used to study wake or jet dynamics [56–58]. The mesh is composed on non-uniformly distributed hexahedral elements which are mostly concentrated around the cylindrical cavity and near the axis $y=0$ around which the wake eventually develops. Additionally, we have taken care in adding thin boundary elements around all boundaries of the cylindrical cavity (of thickness comparable with $\sqrt{\mathrm{E}}$ to properly resolve Ekman boundary layers inside the cavity) and the bottom horizontal channel wall, ensuring a proper resolution of the sharp transition between the stress-free channel and the no-slip boundaries. The number of elements varies between 9408 and up to 13 488 depending on the height of the cylindrical obstacle. Inside each element, the solution is approximated by polynomials of degree N. The degree of the polynomials was varied from $N=7$ up to $N=15$ for the lowest Ekman number. Numerical convergence of the solutions presented here was checked by gradually increasing this polynomial degree. We used a third order time-stepper which implicitly solves for viscous terms while the Coriolis acceleration was solved explicitly. Solutions are dealiased using the standard 3/2 rule.

2. Results

In this section, we discuss the numerical results by first describing qualitatively the transition between a lee wake of inertial waves at high Rossby and a Taylor column at lower Rossby number (Section 2.1). In Section 2.2 we describe the bifurcation of the steady wake of the Taylor column to vortex shedding. We then present in Section 2.3 the wake stability diagram for various Reynolds and Rossby numbers and for the particular case of the cylindrical depression with $h = -1$. We then discuss different properties of the base equilibrium flow below the onset of the instability, from differences between the three-dimensional rotating flow and the analogous two-dimensional non-rotating flow (Section 2.4) to the length of the recirculation bubble behind the obstacle (Section 2.5).

2.1. *Transition between a lee wake and a Taylor column*

While not the main objective of this paper, it is natural to start by describing the gradual transition from a lee wake of inertial waves and a Taylor column [59], which is expected when $\mathrm{Ro}\,\lambda_z/|h| \approx 1$ (see [36,37,39]). In our case with $\lambda_z = 4$ and $|h| = 1$, the transitional Rossby number is expected to be $\mathrm{Ro} \approx 1/4$. We show in Figure 2 the streamwise component of the velocity u_x in various

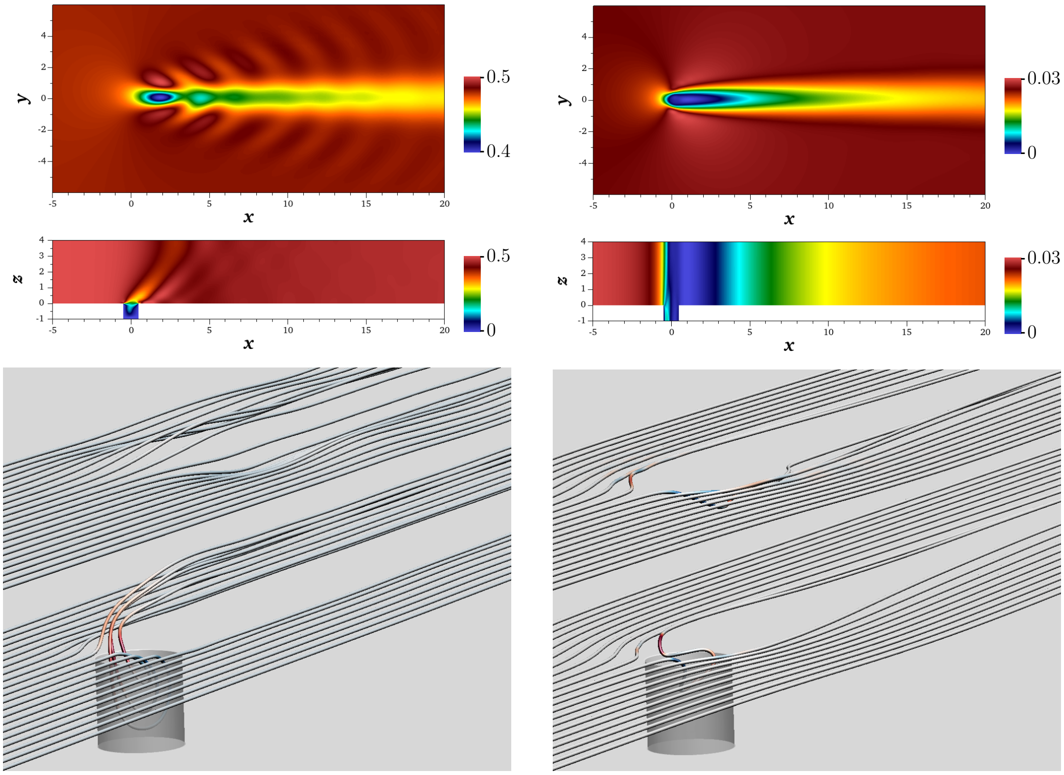

Figure 2. Comparison between wakes at Re = 50 and Ro = 0.5 (left) and Ro = 0.03 (right). The streamwise velocity component is shown on a horizontal slice located at mid-height $z = 2$ (top) and on a vertical slice located at $y = 0$ (middle). We show (bottom) streamlines initiated at two different heights (very close to the bottom of the channel and at mid-height $z = 2$) and colored with the vertical velocity component. While the high Rossby number case is characterized by weak perturbations of the imposed flow, the low Rossby number case clearly creates a Taylor column in the form of a depth-invariant wake.

planes for Re = 50 and two Rossby numbers, Ro = 0.5 and Ro = 0.03, clearly above and below the expected transition at Ro ≈ 1/4. Clearly, at larger Rossby numbers, one observes a lee wake of inertial waves radiated from the cylindrical perturbation. In that case, the advection by the mean imposed flow is comparable with the group velocity of inertial waves leading to the characteristic wave pattern which is stationary at this low Reynolds number of Re = 50. This type of inertial wave lee wake has for example been observed on top of a hemispherical obstacle by [37].

As the Rossby number is reduced, the classical transition toward a vertical free shear layer named Taylor column is observed. While we still observe a remnant of the lee wake of inertial waves, the dominant response is now in the form of a depth invariant flow vertically aligned with the bottom topography. At this Reynolds number, inertia is not completely negligible at the scale of the cylindrical cavity and we clearly observed a wake behind the Taylor column. The stability of this wake, and in particular its convergence towards the classical 2D wake behind a solid cylinder without background rotation, is the focus of the rest of this paper.

2.2. *Bifurcation towards a vortex street for* Ro = 0.03

Before systematically varying the control parameters, let us first fix the Rossby number to a value low enough to sustain a Taylor column, say Ro = 0.03. Figure 3 shows an example of the computed vertical vorticity field in the wake of the Taylor column for Ro = 0.03 and a Reynolds number Re = 65, once the vortex sheet has reached a quasi-stationary state.

As shown in Figure 3, an alternating vortex street forms downstream of the Taylor column despite the absence of an actual solid obstacle, which motivates the term "phantom wake". It closely resembles the classical Bénard–von Kármán wake. The typical spacing between vortices is a classical quantity used to characterize the global structure of a vortex street. In particular, Williamson [52] found a typical distance between two successive vortices of the same sign of $\lambda/D \approx 6.2$ at Re = 65, which is in excellent agreement with the value measured from the local vorticity maxima in Figure 3, namely $\lambda/D \approx 5.95$–6.1. Starting below the instability threshold and gradually increasing the Reynolds number, our first objective is to characterize the bifurcation from a stationary Taylor column to an oscillatory wake, and to compare it with the transition towards vortex shedding classically observed behind a solid cylindrical obstacle. Note that the very existence of a global mode with a unique frequency is itself non-trivial, as it involves the emergence of a wave-maker somewhere in this spatially developing flow [60]. As emphasized in the introduction, an extensive body of literature has been devoted to the Bénard–von Kármán wake. However, it was not until the 1980s and 1990s that the nature of the bifurcation itself

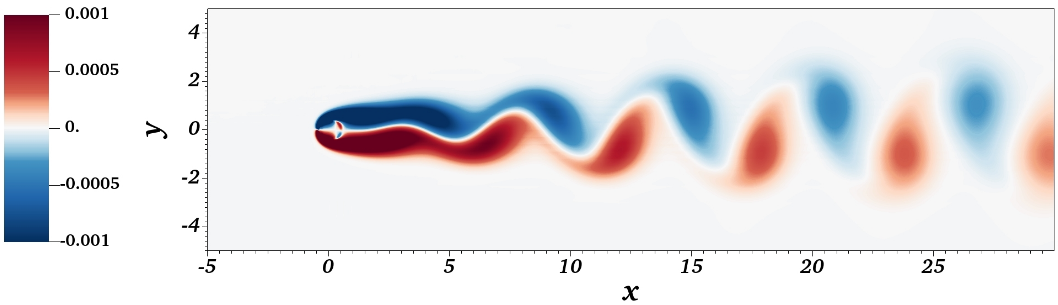

Figure 3. Visualization of the vertical vorticity field (scaled by the rotation rate Ω) in the phantom wake of the Taylor column for Ro = 0.03 and Re = 65 and a cavity with $h = -1$. The plane is located at mid-height $z = 2$ and we only show a small fraction of the whole domain. As can be seen, a vortex street, typical of the classical non-rotating Bénard–von Kármán vortex street is formed in the wake of the column.

was explicitly investigated. In particular, Provansal et al. [6] demonstrated experimentally that the onset of the oscillatory wake occurs through a Hopf bifurcation, which was later confirmed numerically [7]. Although the shedding frequency had been measured long before [52,61,62], it was only in 2006 that Barkley [9] successfully predicted this frequency using a linear stability analysis of the mean flow.

In order to estimate the vortex shedding frequency, we compute the temporal Fourier spectrum of horizontal velocity u_x signals at different locations within the domain, which all peak at a well-defined frequency. This peak is recorded to compute the typical Strouhal number of the wake defined in our choice of dimensional units by

$$\mathrm{St} = \frac{f}{\mathrm{Ro}}, \tag{11}$$

where f is the dimensionless frequency measured in our simulations. Note that this definition reduces to the standard definition $\mathrm{St} = f^* D/U_0$, where $f^* = f\Omega$ is the dimensional frequency. As shown in Figure 4(a), the Strouhal number-Reynolds number relationship measured here for $\mathrm{Ro} = 0.03$ lies slightly above the classical curve. Laws giving St as a function of Re for the 2D classical wake are taken from Wesfreid [5]. The fact that the Strouhal number is generally larger in the rotating case was already observed [26,27,63]. Note that, for this Rossby number, the instability threshold is already shifted toward higher values. As will be shown later, the onset of vortex shedding is in fact a function of the Rossby number.

Figure 4(b) illustrates the nonlinear evolution of the characteristic amplitude of the oscillatory phantom wake, taken at a particular point along the x-axis behind the cylindrical obstacle. As in the classical non-rotating Bénard–von Kármán wake, this amplitude scales with the square root of the distance from threshold, consistent with the behavior of a supercritical Hopf bifurcation. This non linear behavior was also fully described by a Landau equation whose parameters were obtained from measurements. In particular, the ratio of the imaginary part of its cubic term to its real part (the Landau constant) was shown to be equal to −2.7 [6,7]. In the present case of the Taylor column wake, we were able to estimate the Landau coefficient by measuring the variation of the oscillation frequency with its amplitude. This analysis yields a value of approximately −3.5, which significantly differs from its 2D non-rotating analogue. This is not surprising since rotation

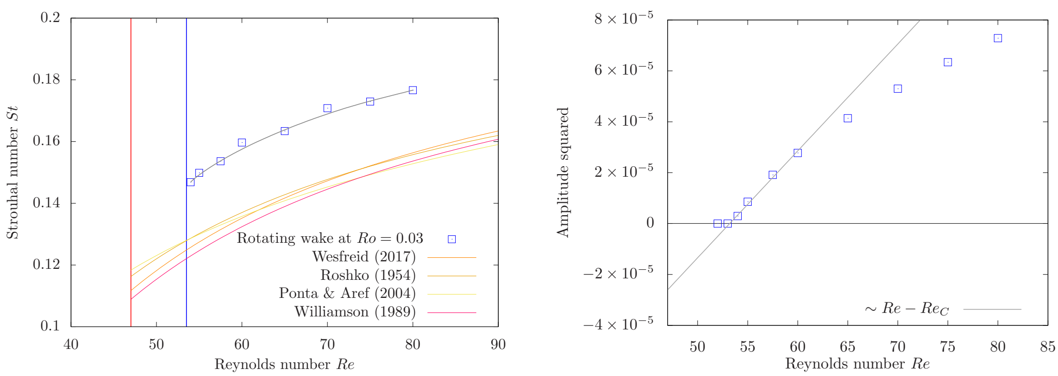

(a) **(b)**

Figure 4. (a) Strouhal number as defined by equation (11) as a function of the Reynolds number. Our phantom wake at $\mathrm{Ro} = 0.03$ is shown with symbols while solid lines correspond to classical fits obtained from classical 2D vortex streets. Vertical lines indicate the critical Reynolds numbers for the onset of the vortex street for each case. (b) Amplitude squared of the transverse velocity component u_y on the symmetry axis $y = 0$ and at the mid-height $z = 2$ averaged behind the cylinder over $x \in [1/2; 8]$. The grey line is a linear fit $\mathrm{Re} - \mathrm{Re_c}$ where the critical value is $\mathrm{Re_c} = 52.8$.

does affect the nonlinear development of the global unstable mode at our finite Rossby number, including its frequency as seen in Figure 4(a). Whether the 2D value of −2.7 is recovered in the limit of vanishing Rossby number remains open. Let us note that this detailed bifurcation analysis is only representative of one small set of data in the large (Ro, Re) domain that we have explored: in particular the measured value of the Landau constant (≈ −3.5, against the classical 2D value of −2.7) is expected to vary with the Rossby number.

2.3. *Systematic variations of Rossby and Reynolds numbers for $h = -1$*

In this section, we systematically vary both Rossby and Reynolds numbers for a fixed depression with height $h = -1$. Each simulation is run until a quasi-stationary state is reached. We use several observables to distinguish between stable and unstable states. The stable wakes are characterized by a flow which is symmetric with respect to the vertical mid-plane $y = 0$. We therefore compute the symmetric and antisymmetric kinetic energies as follows:

$$E_\mathrm{S} = \frac{1}{2V}\iiint \left(u_y(y) - u_y(-y)\right)^2 \mathrm{d}V \qquad \text{and} \qquad E_\mathrm{A} = \frac{1}{2V}\iiint \left(u_y(y) + u_y(-y)\right)^2 \mathrm{d}V, \tag{12}$$

where V is the total volume of the domain. Stable wakes are characterized by $E_\mathrm{S} \gg E_\mathrm{A}$ while unstable wakes are characterized by $E_\mathrm{S} < E_\mathrm{A}$. Alternatively, we compute the temporal Fourier spectrum of horizontal velocity signals at different locations within the domain. Stable wakes are stationary so the spectrum peaks at zero frequency while unstable wakes are oscillating in time so that the spectrum peaks at a non-vanishing frequency. All methods lead to the same separation between stable and unstable states. We show in Figure 5 the full extent of the parameter sweep, where each point corresponds to a direct numerical simulation which has reached a quasi-stationary state. Empty symbols correspond to stable stationary wakes while full symbols correspond to unstable oscillating wakes where the color corresponds to the value of the Strouhal number.

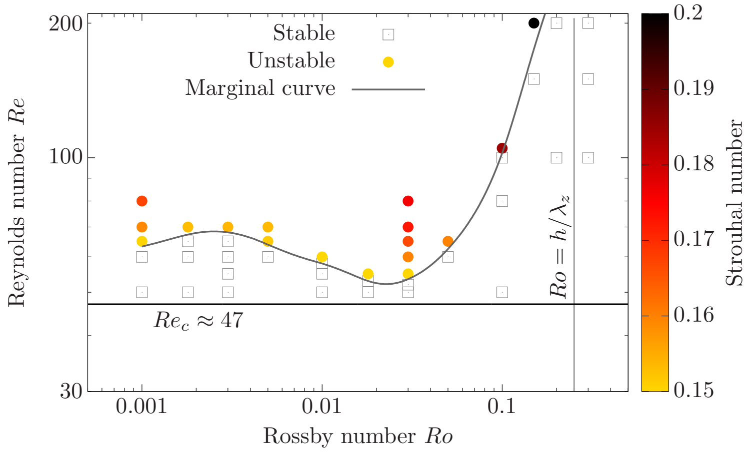

Figure 5. Strouhal number as defined by equation (11) for all simulations with $h = -1$, $\lambda_z = 4$ and various Reynolds and Rossby numbers. Empty symbols correspond to stable case with a stationary flow symmetric around the plane $y = 0$. The continuous grey line correspond to the marginal stability curve estimated by linear interpolation. We recall the critical Reynolds number of Re ≈ 47 of the 2D wake and the theoretical threshold $\mathrm{Ro}\,\lambda_z/h = 1$ for the transition between lee wake of inertial waves and Taylor column. As explained in Section 2.1, this transition occurs when the advection of perturbations by the mean flow becomes comparable to their vertical propagation at the group velocity of inertial waves.

We observe a clear non-monotonic marginal stability curve between stable and unstable wakes.

The value of the Strouhal number for unstable wakes is consistent with the characteristic value associated with a 2D non-rotating wake. In particular, we observe an increase of the Strouhal number as the Reynolds number is increased, which is a well-documented observation for the classical von Kármán vortex street [61,64]. Additionally, we also observe that our Strouhal numbers are slightly larger than their corresponding 2D non-rotating values at the same Reynolds number, which is again consistent with many observations made in rotating wakes [26,27,63]. Finally, we note an interesting analogy between our marginal stability curve and that obtained for porous wakes, with the Rossby number being analogous to the Darcy number in the porous case and which separates unstable and stable wakes [65].

We show again in Figure 5 as a vertical line the critical Rossby $\mathrm{Ro} = h/\lambda_z = 1/4$ which separates lee wakes and Taylor columns [36,37,39]. As expected, we did not observe Taylor columns above this Rossby number and the lee wakes observed above this transition are steady and stable up to the maximum Reynolds number considered here which is $\mathrm{Re} = 200$. While other bifurcation mechanisms may exist for lee wakes at high Rossby and Reynolds numbers, we do not explore this regime here and instead focus exclusively on the bifurcation of Taylor columns occurring when $\mathrm{Ro} < h/\lambda_z = 1/4$. The first instability occurs at $\mathrm{Ro} = 0.15$ for a Reynolds number of $\mathrm{Re} = 200$, far beyond the expected 2D critical Reynolds number of $\mathrm{Re_c} \approx 47$. As the Rossby number is further decreased, the critical Reynolds number decreases and gets closer to the value associated with the classical wake behind a solid cylinder in the absence of confinement effects, $\mathrm{Re} \approx 47$ [6,66]. This is expected since the validity of the Taylor–Proudman theorem is based on neglecting inertia compared to the Coriolis acceleration, which is all the more justified that the Rossby number is small. However, surprisingly, below $\mathrm{Ro} \approx 0.03$, the critical Reynolds number *increases* as the Rossby number is decreased. The local minimum critical Reynolds number of $\mathrm{Re} \approx 53$ is reached for approximately $\mathrm{Ro} \approx 0.02$. This unexpected trend continues down to $\mathrm{Ro} \approx 3 \times 10^{-3}$, after which we recover the more intuitive trend of a critical Reynolds number decreasing with the Rossby number. This non-monotonic convergence between the 3D rotating system and its 2D analogue is unexpected and deserves further consideration.

2.4. *Global base flow difference*

A useful initial observation emerges from comparing the horizontal flow between the 2D system and the rotating 3D system. Figure 6(a) presents the comparison between the reference 2D base flow (top) and the rotating 3D base flow at $\mathrm{Ro} = 10^{-3}$ (bottom). The Reynolds number is $\mathrm{Re} = 50$ in both cases. The 2D reference simulation is performed as follows: we use the same horizontal geometry as in the 3D rotating system, with identical boundary conditions except that an actual solid obstacle with no-slip boundary is now present. The Reynolds number is set to $\mathrm{Re} = 50$, sufficiently low to ensure marginal stability in any 3D configuration (see Figure 5) and to allow the 2D system to reach a steady base flow before any instability develops. We save the base stationary horizontal flow in a domain near the cylinder, repeating the process for each simulation, where the base flow is saved at mid-height $z = \lambda_z/2 = 2$. Note that the following results are unchanged when considering other heights, since the base flow and its associated instability are, to first order, depth-invariant. We then measure the L_2 relative difference between both base flows in a domain around the obstacle defined by $x \in [-2;6]$ and $y \in [-2;2]$, and at mid-height $z = 2$ for the 3D case. We distinguish between the horizontal component, present in both systems, and the vertical component, which only exists in the 3D rotating system. Results are shown in Figure 6(b), where the Rossby number is systematically varied for a fixed Reynolds number $\mathrm{Re} = 50$. While the vertical flow component decreases with the Rossby number, as required for the 3D rotating

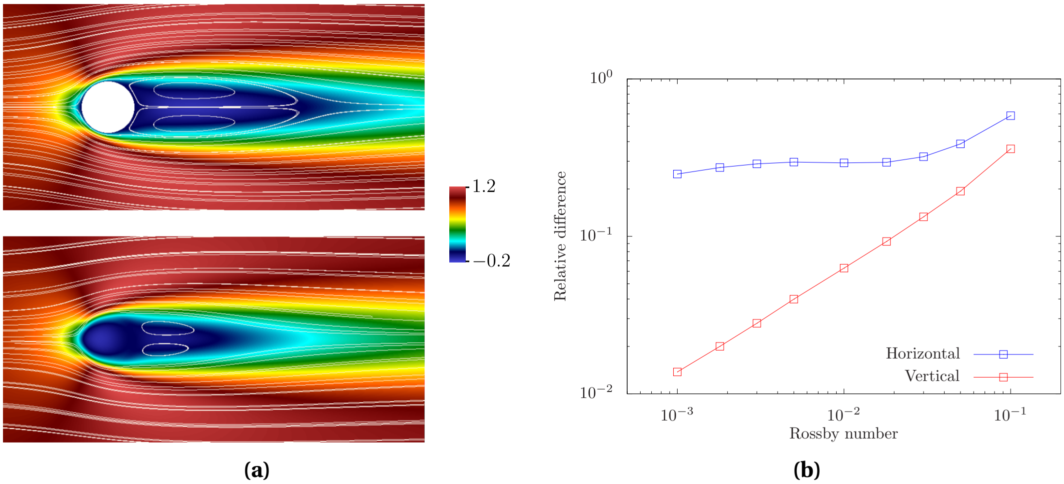

Figure 6. (a) Comparison between the reference 2D base flow (top) and the rotating 3D base flow at $\mathrm{Ro} = 10^{-3}$ (bottom, shown at $z = 2$). The Reynolds number is $\mathrm{Re} = 50$ in both cases and the colors show the streamwise component of the flow (normalised by the Rossby number for the 3D case to be comparable with the 2D case) while white lines correspond to streamlines. (b) L_2 relative difference between the 2D and 3D rotating base flow at $\mathrm{Re} = 50$ and as a function of Rossby. We distinguish between the horizontal components and the vertical component (which is zero in the 2D case).

system to eventually converge toward the 2D system, the horizontal flow does not converge monotonically. The horizontal error follows the same trend as the critical Reynolds number, with a surprising stagnation of the error as the Rossby number decreases from $\mathrm{Ro} \approx 3 \times 10^{-2}$ to $\mathrm{Ro} \approx 5 \times 10^{-3}$. The slow convergence already observed in Figure 5, which could have been related to a non-vanishing vertical velocity around the cylinder, can therefore be explained by focusing on the horizontal flow alone.

2.5. *Recirculation bubble length*

Figure 6(a) already showed a clear difference between the 2D base flow and its rotating 3D analogue. The recirculation bubble length behind the cylinder is much smaller in the 3D rotating configuration than it is in the 2D case. This is more systematically showed in Figure 7 where isocontours of vanishing streamwise velocity $u_x = 0$ are compared at $\mathrm{Re} = 50$. We recall that this recirculation bubble and its spatial structure are responsible for the existence of a global mode through a wave-maker mechanism operating at a well-defined frequency [60]. Again, the 3D rotating results are showed in the mid-plane $z = 2$ for comparison with the 2D results. Clearly, the length of the recirculation bubble, inside which negative streamwise velocities are observed is significantly smaller in the 3D rotating system at all Rossby numbers explored here. Since the rotating wakes are not exactly symmetric around the $y = 0$ plane, as expected due to the finite Rossby numbers considered here, the recirculation length L_{R} is defined and measured as the maximum streamwise position for which we observe a vanishing streamwise velocity, which is not necessarily on the axis $y = 0$ in our rotating cases. The value we obtained with our 2D numerical approach, $L_{\mathrm{R}} \approx 3.42$ (measured from the center of the cylindrical obstacle), is consistent with the typical value of $L_{\mathrm{R}}/D \approx 0.066\,\mathrm{Re}$ which leads to 3.3 for $\mathrm{Re} = 50$ [8,67–69]. The results are shown in Figure 8 where L_{R} is plotted for the various Rossby numbers of Figure 7. Again, we observe this non-monotonic behaviour in the recirculation length, closely matching the non-monotonic trend observed on the critical Reynolds number in Figure 5. Note that,

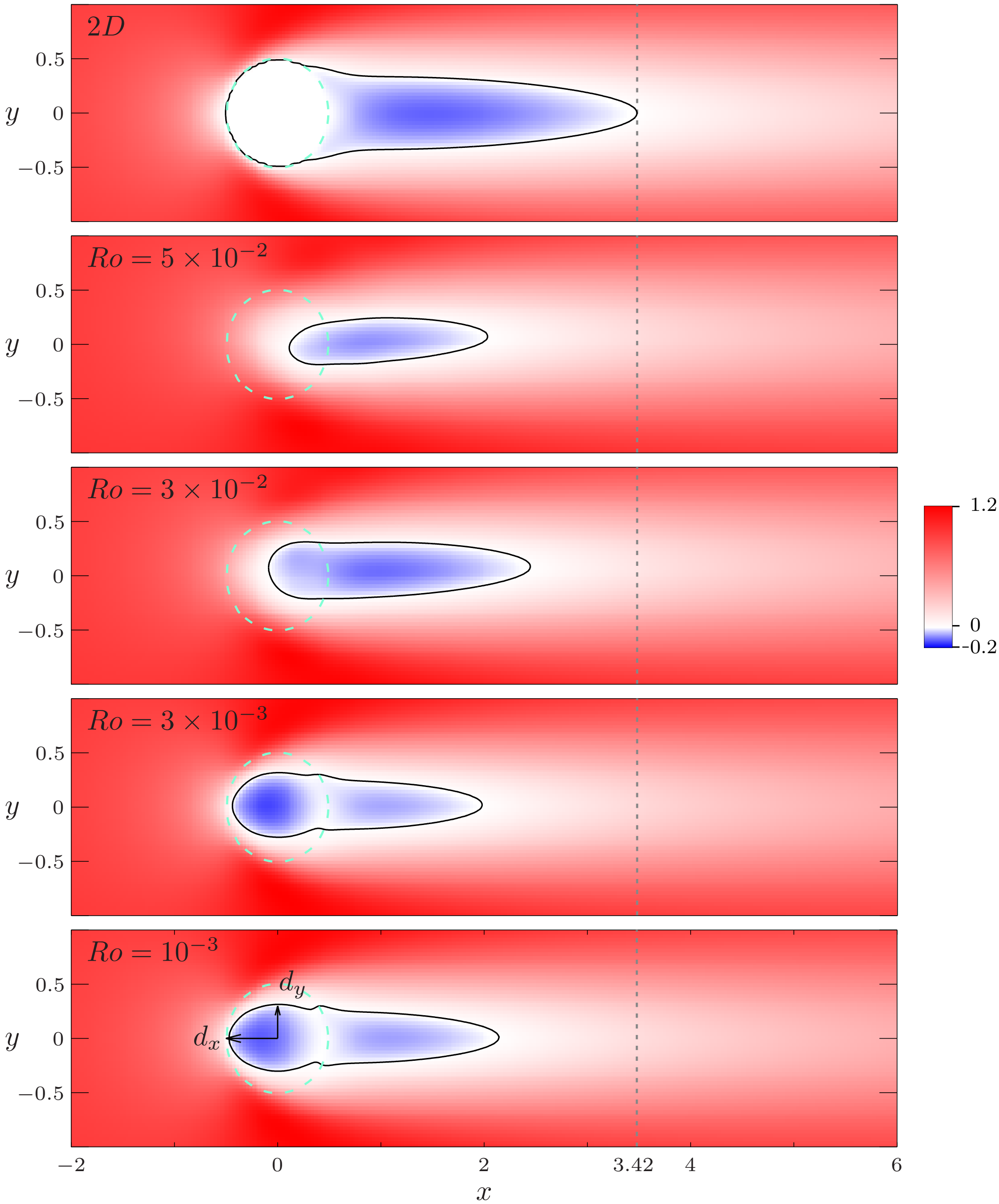

Figure 7. Streamwise velocity component (normalised by the Rossby number for the 3D cases). The black continuous lines correspond to the isocontour of vanishing streamwise velocity. The dotted gray line indicates the length of the recirculation bubble for the 2D case shown on the top panel, $L_R \approx 3.42$. The dash cyan line correspond to the contour of the cylindrical obstacle. The Reynolds number is Re = 50 in all cases while the 2D case (top) is compared to the rotating 3D cases at various Rossby numbers and at mid-height $z = 2$.

consistently with our observation, a shorter recirculation bubble is generally associated with a larger critical Reynolds number [70].

It is also instructive to examine the characteristic shape of the flow around the cylindrical obstacle. While the 2D reference flow exhibits circular streamlines around the leading edge of the cylinder, the contours presented in Figure 7 adopt a more elliptical shape for the 3D rotating cases. We observe a rapid convergence of the stagnation point toward its expected position at $x = -1/2$ and $y = 0$ in our dimensionless units. However, over the same range of Rossby numbers, the characteristic extent of the flow in the y direction changes only slightly. This behavior is evident in Figure 7 and is further quantified in Figure 8(b). To characterize these features, we compute two length scales d_x and d_y. The location of the stagnation point is determined as the minimum streamwise position at which the streamwise velocity vanishes. The absolute value of this position is denoted as d_x. In the transverse direction, we measure the maximum and minimum y coordinates of the contours shown in Figure 7. The average of these values is referred to as d_y and is presented alongside d_x in Figure 8(b). While d_x rapidly converges toward its expected value of 1/2, the convergence of d_y is much slower and non-monotonic. This results in an effective base flow with elliptical streamlines inside the obstacle. This observation is again consistent with a higher critical Reynolds number, as it is known that increasing the ellipticity of an obstacle delays the onset of the Bénard–von Kármán vortex street behind elliptical bodies [66].

In all these observations, we observe that below $\mathrm{Ro} \approx 3\times10^{-3}$, the critical Reynolds number, the recirculation length and the characteristic shape of the flow around the obstacle all seem to converge towards their 2D counterparts. This convergence however appears to be very slow, and even for the lowest Rossby number achieved here, $\mathrm{Ro} = 10^{-3}$, the critical Reynolds number is $\mathrm{Re} \approx 63$ which is still far from the 2D value of $\mathrm{Re} \approx 47$. Whether the convergence between the two problems remains monotonous below this Rossby number remains to be verified. Note finally that the main difference between the two problems appears to be related to the effective size of the obstacle, which is smaller in the three-dimensional rotating case than in its two-dimensional counterpart, as observed in Figures 6 and 7. While we have not attempted to compensate for this effect in the present study, future work could investigate whether the remaining discrepancies persist once this first-order effect is compensated for, for example by adjusting the obstacle diameter.

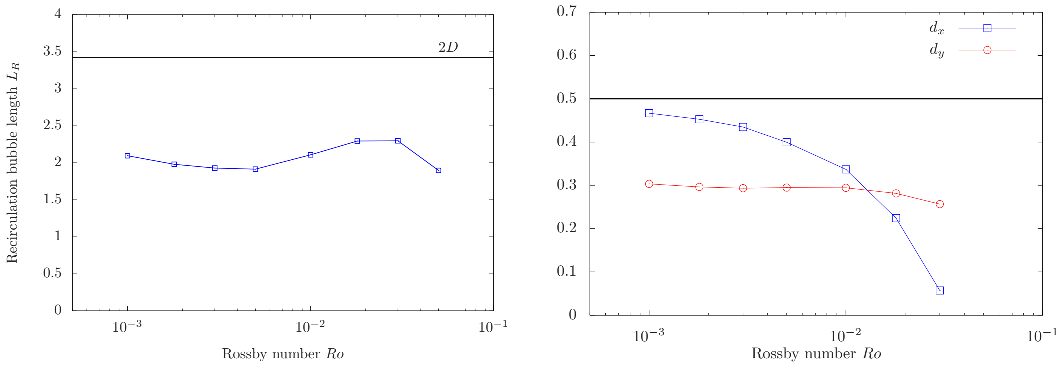

(a) **(b)**

Figure 8. (a) Recirculation bubble length L_R as a function of the Rossby number at Re = 50. It is measured as the maximum streamwise position for which we observe a vanishing streamwise velocity. The 2D reference value at the same Reynolds number is recalled as a horizontal black line. (b) Characteristic sizes of the flow around the cylinder at different Rossby numbers and for Re = 50.

2.6. *Role of the geometric parameters*

Finally, let us briefly discuss the difference between a depression or cavity ($h < 0$) and a protruding obstacle ($h > 0$). The depression case discussed up to now is of course the most dramatic example of a wake behind a Taylor column since there is no solid obstacle opposing the flow inside the channel. The only dynamical constraint originates from the impossibility for the flow to pass over the cavity, which would violate the Taylor–Proudman theorem. When a finite obstacle protrudes inside the channel, a fraction of the imposed flow has to go around the object independently of the Rossby number. The Taylor–Proudman number then ensures that a Taylor column forms above the obstacle. These two configurations are not symmetric. The cavity can be as deep as one wants while the obstacle height is at most the channel height. In that case, and in the absence of Ekman boundary layers along the boundary of the channel as it is the case here, we expect to fully recover the analogy between the 2D and the 3D rotating system. This is because the Coriolis acceleration can be absorbed into the pressure gradient in that case since the 3D rotating system is now invariant along the rotation axis. We have done such simulations which correspond in our case to $h = \lambda_z = 4$ so that the cylinder now extends across the whole channel. As shown in Figure 9, we have run several simulations at $\mathrm{Ro} = 3 \times 10^{-3}$ and found that the critical Reynolds number for the vortex street lies somewhere between Re = 45 and Re = 50, which is consistent with the discussion above.

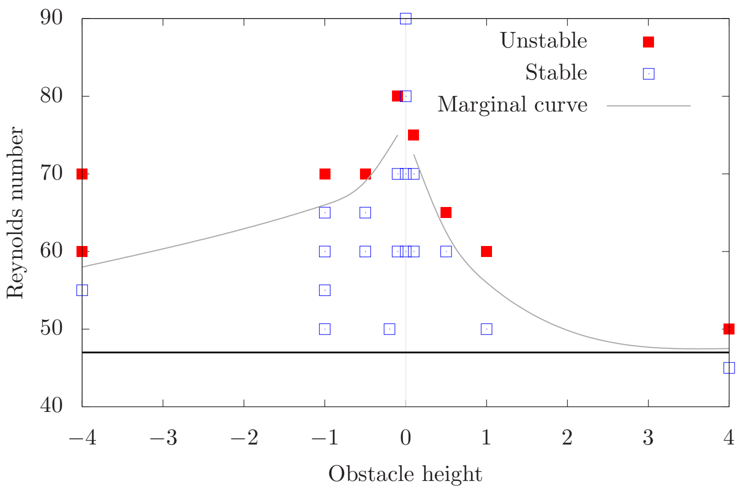

Figure 9. Critical Reynolds number for $\mathrm{Ro} = 3 \times 10^{-3}$ as a function of the obstacle height. Negative values correspond to the height of the cavity outside the channel while positive values correspond to the height of the obstacle protruding inside the channel.

We also varied systematically the height of the obstacle between $h = -4$ and $h = 4$ (the depth-invariant cylindrical obstacle) and for a Rossby number of $\mathrm{Ro} = 3 \times 10^{-3}$. The case $h = 0$, where we impose a no-slip boundary condition inside a unit circle along a stress-free channel without topography, remained stable for all Reynolds number investigated up to Re = 200. For the Rossby number considered here of $\mathrm{Ro} = 3 \times 10^{-3}$, the obstacle case ($h > 0$) has a lower critical Reynolds number than its depression counterpart ($h < 0$). Note however that the non-monotonous convergence with the Rossby number discussed earlier for the case of a depression remains true for the case of the obstacle, at least for the symmetric case $h = 1$ which we systematically explored (not shown). While this remains speculative at this stage, we believe that the asymmetry between the protruding solid obstacle and the cavity originates from the different pressure fields generated by the two configurations. In the former case, the flow cannot penetrate the solid obstacle, resulting in a direct perturbation of the pressure field. In contrast, for the cavity, the phantom obstacle forms more indirectly through the propagation of inertial waves, since there is no physical obstacle partially blocking the flow through the channel.

3. Conclusion

We investigated the instability of the wake formed behind a Taylor column within a rapidly rotating channel subjected to an imposed flow. To facilitate convergence between the classical 2D wake problem behind a solid cylinder and the 3D rotating problem involving cavities, we considered a stress-free channel, thereby avoiding complications associated with Ekman boundary layers. Under these conditions, we observed a non-monotonic convergence of the 3D rotating problem toward the 2D case. As the Rossby number decreases, a vortical sheet invariant along the rotation axis emerges. We then observe a transition from the steady wake of the Taylor column to an alternating vortex street through a Hopf bifurcation, in a manner similar to the classical Bénard–von Kármán vortex street. This transition occurs despite the absence of any physical obstacle within the channel, giving rise to the term “phantom” wake. Because these unstable wakes arise from the Taylor–Proudman constraint, we refer to them as Bénard–von Kármán–Taylor–Proudman phantom wakes.

At this stage, the mechanism underlying the emergence of an elliptical Taylor column surrounding the cavity, rather than a circular structure consistent with the cavity geometry, remains unresolved. The leading edge appears to play a more significant role in the formation of the Taylor column than the lateral sides, which is not entirely unexpected. This may be attributed to the topographic step introduced by the cavity being more pronounced at the leading edge, where the flow is oriented normal to the cavity boundary, whereas along the lateral sides the imposed flow remains largely tangential. Consequently, the overall cavity geometry is likely to exert a strong influence on the resulting flow structure. In support of this, our first analysis (not shown here) of a square cavity indicates that the relative discrepancies in both the critical Reynolds number and the recirculation length between the three-dimensional rotating configuration and its two-dimensional analogue are smaller than those observed for a solid circular cylinder. Although further systematic investigation is required, these preliminary results suggest that cavity geometry, possibly through its influence on the generation of inertial waves, may play a significant role and deserve further investigation in future studies.

Acknowledgments

Centre de Calcul Intensif d’Aix-Marseille is acknowledged for granting access to its high performance computing resources. This work was granted access to the HPC resources of IDRIS under the allocation 2026-A0200407543 made by GENCI.

Declaration of interests

The authors do not work for, advise, own shares in, or receive funds from any organization that could benefit from this article, and have declared no affiliations other than their research organizations.

References

[1] H. Bénard, "Formation périodique des centres de giration à l'arrière d'un obstacle en mouvement", *C. R. Acad. Sci. Paris* **147** (1908), pp. 839–842.

[2] H. Bénard, "Étude cinématographique des remous et des rides produits par la translation d'un obstacle", *C. R. Acad. Sci. Paris* **147** (1908), pp. 970–972.

[3] T. Von Kármán, "Über den Mechanismus des Widerstandes, den ein bewegter Körper in einer Flüssigkeit erfährt", *Nachr. Ges. Wiss. Göttingen, Math.-Phys. Kl.* **1911** (1911), pp. 509–517.

[4] T. Von Kármán, "Über den Mechanismus des Flussigkeits- und Luftwiderstandes", *Phys. Zeit.* **13** (1912), pp. 49–59.

[5] J.-E. Wesfreid, "Henri Bénard: thermal convection and vortex shedding", *Comptes Rendus. Mécanique* **345** (2017), no. 7, pp. 446–466.

[6] M. Provansal, C. Mathis and L. Boyer, "Bénard-von Kármán instability: transient and forced regimes", *J. Fluid Mech.* **182** (1987), pp. 1–22.

[7] J. Dušek, P. Le Gal and P. Fraunié, "A numerical and theoretical study of the first Hopf bifurcation in a cylinder wake", *J. Fluid Mech.* **264** (1994), pp. 59–80.

[8] B. J. A. Zielinska, S. Goujon-Durand, J. Dušek and J.-E. Wesfreid, "Strongly Nonlinear Effect in Unstable Wakes", *Phys. Rev. Lett.* **79** (1997), pp. 3893–3896.

[9] D. Barkley, "Linear analysis of the cylinder wake mean flow", *Europhys. Lett.* **75** (2006), no. 5, pp. 750–756.

[10] G. I. Taylor, "Motion of solids in fluids when the flow is not irrotational", *Philos. Trans. R. Soc. Lond., Ser. A, Contain. Pap. Math. Phys. Character* **93** (1917), no. 648, pp. 99–113.

[11] J. Proudman, "On the motion of solids in a liquid possessing vorticity", *Philos. Trans. R. Soc. Lond., Ser. A, Contain. Pap. Math. Phys. Character* **92** (1916), no. 642, pp. 408–424.

[12] S. S. Hough, "On the application of harmonic analysis to the dynamical theory of the tides. Part I: On Laplace's oscillations of the first species and on the dynamics of ocean currents", *Proc. R. Soc. Lond.* **61** (1897), no. 369–377, pp. 236–238.

[13] O. U. Velasco Fuentes, "Kelvin's discovery of Taylor columns", *Eur. J. Mech. B Fluids* **28** (2009), no. 3, pp. 469–472.

[14] G. I. Taylor, "Experiments on the motion of solid bodies in rotating fluids", *Philos. Trans. R. Soc. Lond., Ser. A, Contain. Pap. Math. Phys. Character* **104** (1923), no. 725, pp. 213–218.

[15] J. Arístegui, P. Sangrá, S. Hernández-León, M. Cantón, A. Hernández-Guerra and J. L. Kerling, "Island-induced eddies in the Canary islands", *Deep Sea Res. Part I* **41** (1994), no. 10, pp. 1509–1525.

[16] R. M. A. Caldeira, S. Groom, P. Miller, D. Pilgrim and N. P. Nezlin, "Sea-surface signatures of the island mass effect phenomena around Madeira Island, Northeast Atlantic", *Remote Sens. Environ.* **80** (2002), no. 2, pp. 336–360.

[17] J. Vidal, J. Noir, D. Cébron, F. Burmann, R. Monville, V. Giraud and Y. Charles, "Geophysical flows over topography, a playground for laboratory experiments", *Comptes Rendus. Physique* **25** (2024), pp. 183–234.

[18] F. P. Bretherton, "The time-dependent motion due to a cylinder moving in an unbounded rotating or stratified fluid", *J. Fluid Mech.* **28** (1967), no. 3, pp. 545–570.

[19] H. K. Cheng and E. R. Johnson, "Inertial waves above an obstacle in an unbounded, rapidly rotating fluid", *Proc. R. Soc. Lond., A, Math. Phys. Eng. Sci.* **383** (1982), no. 1784, pp. 71–87.

[20] T. Aurégan, T. Bonometti and J. Magnaudet, "Flow past a sphere translating along the axis of a rotating fluid: revisiting numerically Maxworthy's experiments", *J. Fluid Mech.* **967** (2023), article no. A25.

[21] E. R. Johnson, "The effects of obstacle shape and viscosity in deep rotating flow over finite-height topography", *J. Fluid Mech.* **120** (1982), pp. 359–383.

[22] N. Machicoane, V. Labarre, B. Voisin, F. Moisy and P.-P. Cortet, "Wake of inertial waves of a horizontal cylinder in horizontal translation", *Phys. Rev. Fluids* **3** (2018), no. 3, article no. 034801 (28 pages).

[23] P. Meunier, "Stratified wake of a tilted cylinder. Part 1: Suppression of a von Kármán vortex street", *J. Fluid Mech.* **699** (2012), pp. 174–197.

[24] D. L. Boyer, "Flow Past a Right Circular Cylinder in a Rotating Frame", *J. Fluids Eng.* **92** (1970), no. 3, pp. 430–435.

[25] D. L. Boyer and P. A. Davies, "Flow past a circular cylinder on a β-plane", *Philos. Trans. R. Soc. Lond., Ser. A* **306** (1982), no. 1496, pp. 533–556.

[26] D. L. Boyer and M. L. Kmetz, "Vortex shedding in rotating flows", *Geophys. Astrophys. Fluid Dyn.* **26** (1983), no. 1–2, pp. 51–83.

[27] D. L. Boyer, M. L. Kmetz, L. Smathers, G. Chabert d'Hieres and H. Didelle, "Rotating open channel flow past right circular cylinders", *Geophys. Astrophys. Fluid Dyn.* **30** (1984), no. 4, pp. 271–304.

[28] S. Teinturier, A. Stegner, H. Didelle and S. Viboud, "Small-scale instabilities of an island wake flow in a rotating shallow-water layer", *Dyn. Atmos. Oceans* **49** (2010), no. 1, pp. 1–24.

[29] T. Matsuura and T. Yamagata, "A numerical study of a viscous flow past a right circular cylinder on a β-plane", *Geophys. Astrophys. Fluid Dyn.* **37** (1986), no. 1–2, pp. 129–164.

[30] A. Stegner, T. Pichon and M. Beunier, "Elliptical-inertial instability of rotating Kármán vortex streets", *Phys. Fluids* **17** (2005), no. 6, pp. 1–10.

[31] G. I. Taylor, "The motion of a sphere in a rotating liquid", *Philos. Trans. R. Soc. Lond., Ser. A, Contain. Pap. Math. Phys. Character* **102** (1922), no. 715, pp. 180–189.

[32] K. Stewartson, "On the motion of a sphere along the axis of a rotating fluid", *Q. J. Mech. Appl. Math.* **11** (1958), no. 1, pp. 39–51.

[33] D. W. Moore and P. G. Saffman, "The rise of a body through a rotating fluid in a container of finite length", *J. Fluid Mech.* **31** (1968), no. 4, pp. 635–642.

[34] T. Maxworthy, "The flow created by a sphere moving along the axis of a rotating, slightly-viscous fluid", *J. Fluid Mech.* **40** (1970), no. 3, pp. 453–479.

[35] J. W. M. Bush, H. A. Stone and J. Bloxham, "Axial drop motion in rotating fluids", *J. Fluid Mech.* **282** (1995), pp. 247–278.

[36] R. Hide and A. Ibbetson, "An experimental study of "Taylor columns"", *Icarus* **5** (1966), no. 1, pp. 279–290.

[37] K. E. Heikes and T. Maxworthy, "Observations of inertial waves in a homogeneous rotating fluid", *J. Fluid Mech.* **125** (1982), pp. 319–345.

[38] A. P. Ingersoll, "Inertial Taylor columns and Jupiter's great red spot", *J. Atmos. Sci.* **26** (1969), no. 4, pp. 744–752.

[39] H. E. Huppert, "Some remarks on the initiation of inertial Taylor columns", *J. Fluid Mech.* **67** (1975), no. 2, pp. 397–412.

[40] P. J. Mason and R. I. Sykes, "A numerical study of rapidly rotating flow over surface-mounted obstacles", *J. Fluid Mech.* **111** (1981), pp. 175–195.

[41] K. Stewartson and H. K. Cheng, "On the structure of inertial waves produced by an obstacle in a deep, rotating container", *J. Fluid Mech.* **91** (1979), no. 3, pp. 415–432.

[42] M. Takematsu and T. Kita, "Vortex Shedding from "Taylor columns"", *J. Phys. Soc. Japan* **45** (1978), no. 5, pp. 1781–1782.

[43] D. L. Boyer, P. A. Davies and W. R. Holland, "Rotating flow past disks and cylindrical depressions", *J. Fluid Mech.* **141** (1984), pp. 67–95.

[44] H. A. Khaledi and H. I. Andersson, "On vortex streets behind Taylor columns", *Phys. Lett. A* **374** (2010), pp. 4517–4522.

[45] S. J. Jacobs, "The Taylor column problem", *J. Fluid Mech.* **20** (1964), no. 4, pp. 581–591.

[46] J. David, A. Walker and K. Stewartson, "The flow past a circular cylinder in a rotating frame", *Z. Angew. Math. Phys.* **23** (1972), no. 5, pp. 745–752.

[47] J. D. A. Walker and K. Stewartson, "Separation and the Taylor-column problem for a hemisphere", *J. Fluid Mech.* **66** (1974), no. 4, pp. 767–789.

[48] L.-O. Merkine and A. Solan, "The separation of flow past a cylinder in a rotating system", *J. Fluid Mech.* **92** (1979), no. 2, pp. 381–392.

[49] Y. D. Afanasyev, P. B. Rhines and E. G. Lindahl, "Vortices and Rossby waves in cylinder wakes on a parabolic β-plane observed by altimetric imaging velocimetry", *Phys. Fluids* **20** (2008), no. 8, article no. 086604.

[50] O. Posdziech and R. Grundmann, "A systematic approach to the numerical calculation of fundamental quantities of the two-dimensional flow over a circular cylinder", *J. Fluids Struct.* **23** (2007), no. 3, pp. 479–499.

[51] R. Gautier, D. Biau and E. Lamballais, "A reference solution of the flow over a circular cylinder at Re = 40", *Comput. Fluids* **75** (2013), pp. 103–111.

[52] C. H. K. Williamson, "Oblique and parallel modes of vortex shedding in the wake of a circular cylinder at low Reynolds numbers", *J. Fluid Mech.* **206** (1989), pp. 579–627.

[53] P. F. Fischer, "An Overlapping Schwarz Method for Spectral Element Solution of the Incompressible Navier–Stokes Equations", *J. Comput. Phys.* **133** (1997), pp. 84–101.

[54] M. O. Deville, P. F. Fischer and E. H. Mund, *High-Order Methods for Incompressible Fluid Flow*, Cambridge University Press, 2002.

[55] P. Fischer, J. Lottes and S. Kerkemeier, *Nek5000: open source spectral element CFD solver*, v19.0, 2008. Online at http://nek5000.mcs.anl.gov.

[56] R. Vinuesa, P. Schlatter, J. Malm, C. Mavriplis and D. S. Henningson, "Direct numerical simulation of the flow around a wall-mounted square cylinder under various inflow conditions", *J. Turbul.* **16** (2015), no. 6, pp. 555–587.

[57] G. Chauvat, A. Peplinski, D. S. Henningson and A. Hanifi, "Global linear analysis of a jet in cross-flow at low velocity ratios", *J. Fluid Mech.* **889** (2020), article no. A12 (21 pages).

[58] D. Massaro, A. Peplinski and P. Schlatter, "The flow around a stepped cylinder with turbulent wake and stable shear layer", *J. Fluid Mech.* **977** (2023), article no. A3 (32 pages).

[59] P. A. Davidson, *The Dynamics of Rotating Fluids*, Oxford University Press, 2024.

[60] P. Huerre and P. A. Monkewitz, "Local and Global Instabilities in Spatially Developing Flows", *Annu. Rev. Fluid Mech.* **22** (1990), pp. 473–537.

[61] A. Roshko, *On the development of turbulent wakes from vortex streets*, NACA technical note, National Advisory Committee for Aeronautics, no. NACA-TR-1191, 1954.

[62] F. L. Ponta and H. Aref, "Strouhal–Reynolds Number Relationship for Vortex Streets", *Phys. Rev. Lett.* **93** (2004), article no. 084501 (4 pages).

[63] H. A. Khaledi, M. Barri and H. I. Andersson, "On the stabilizing effect of the Coriolis force on the turbulent wake of a normal flat plate", *Phys. Fluids* **21** (2009), no. 9, article no. 095104.

[64] M. Hammache and M. Gharib, "An experimental study of the parallel and oblique vortex shedding from circular cylinders", *J. Fluid Mech.* **232** (1991), pp. 567–590.

[65] F. Caruso Lombardi, A. Bongarzone, G. A. Zampogna, F. Gallaire, S. Camarri and P. G. Ledda, "Von Kármán vortex street past a permeable circular cylinder: Two-dimensional flow and dynamic-mode-decomposition-based secondary stability analysis", *Phys. Rev. Fluids* **8** (2023), no. 8, article no. 083901 (29 pages).

[66] C. P. Jackson, "A finite-element study of the onset of vortex shedding in flow past variously shaped bodies", *J. Fluid Mech.* **182** (1987), pp. 23–45.

[67] S. Taneda, "Experimental Investigation of the Wakes behind Cylinders and Plates at Low Reynolds Numbers", *J. Phys. Soc. Japan* **11** (1956), no. 3, pp. 302–307.

[68] M. Coutanceau and R. Bouard, "Experimental determination of the main features of the viscous flow in the wake of a circular cylinder in uniform translation. Part 1: Steady flow", *J. Fluid Mech.* **79** (1977), no. 2, pp. 231–256.

[69] B. Fornberg, "A numerical study of steady viscous flow past a circular cylinder", *J. Fluid Mech.* **98** (1980), no. 4, pp. 819–855.

[70] E. Boujo and F. Gallaire, "Controlled reattachment in separated flows: a variational approach to recirculation length reduction", *J. Fluid Mech.* **742** (2014), pp. 618–635.